Chemical Geology 674 (2025) 122561

Contents lists available at ScienceDirect

Chemical Geology

journal homepage: www.elsevier.com/locate/chemgeo

Fe-dependent structural evolution of peralkaline soda aluminosilicate glasses: Iron speciation *vs.* glass transition

Michele Cassetta [a,b,*], Emanuele De Bona [c], Alessia Sambugaro [b], Francesco Enrichi [b], Nicola Daldosso [b], Beatrice Giannetta [d], Claudio Zaccone [e,f], Mattia Biesuz [c], Vincenzo M. Sglavo [c], Renat Almeev [g], Luca Nodari [h], Daniele Giordano [a,i,j], Gino Mariotto [b]

[a] Department of Earth Science, University of Torino, I-10125 Torino, Italy
[b] Department of Engineering for Innovation Medicine, University of Verona, I-37134 Verona, Italy
[c] Department of Industrial Engineering, University of Trento, I-38122 Trento, Italy
[d] Department of the Sciences of Agriculture, Food, Natural Resources and Engineering, University of Foggia, I-71100 Foggia, Italy
[e] Department of Biotechnology, University of Verona, I-37134 Verona, Italy
[f] National Institute of Geophysics and Volcanology (INGV), I-00143 Roma, Italy
[g] Institute of Earth System Sciences, Leibniz University of Hannover, D-30167 Hannover, Germany
[h] Institute of Condensed Matter Chemistry and Technologies for Energy, National Research Council (ICMATE-CNR), I-35127 Padova, Italy
[i] Institute of Geosciences and Earth Resources, National Research Council of Italy (CNR-IGG), I-56127 Pisa, Italy
[j] Istituto di Scienza, Tecnologia e Sostenibilità per lo Sviluppo dei Materiali Ceramici (CNR-ISSMC), I-48018 Faenza, Italy

ARTICLE INFO

Editor: Claudia Romano

Keywords:
Iron
Soda Aluminosilicate Glasses
Glass transition
Mössbauer
Raman
FTIR
ATR

ABSTRACT

The incorporation of iron into peralkaline silicate glasses significantly impacts their structural and thermal properties. Here we investigate how addition of iron influences the network connectivity (short- and medium-range order) and glass transition temperature (T_g) with particular regard to the iron speciation and the Fe^{2+} and Fe^{3+} coordination state. We also found a sort of tipping point in iron concentration beyond which the short-range structures evolve linearly with density while the medium-range structure deviates from linearity. This behavior seems related to a re-enrichment of tetrahedral units triggered by iron self-compensation effect explaining the observed jump in T_g.

1. Introduction

Iron-bearing silicate glasses hold particular significance in petro-volcanological processes (oxidation, clustering, crystallization, transport mechanisms), on a continuous length scale, from deep into the crust to eruption (Chevrel et al., 2013; Stabile et al., 2016; Wilke, 2005; Le Losq et al., 2021) whilst arousing particular interest in industrial perspectives (Chinnam et al., 2013). The characterization of their short- to medium-range order is a key step towards the understanding contribution of iron to the physico-chemical properties of the glass. In particular, the ternary Na_2O–Al_2O_3–SiO_2 (NAS) system has deep implications for both manufacturing processes and geology. NAS, indeed, makes up to about 80 % of andesitic to rhyolitic volcanic materials and their magmatic counterparts (Mysen and Richet, 2005). Usually, NAS systems are also chosen as simple model series of glass-forming melts to investigate changes in physical properties upon structural modifications (Antoni et al., 2004; Hehlen and Neuville, 2020; Le Losq et al., 2014). For instance, the viscosity increases by increasing the ratio Al/(Al + Na) from 0 to 0.5 (peralkaline), achieving a maximum when Al/(Al + Na) ≈ 0.5 (peraluminous) and eventually dropping down for Al/(Al + Na) > 0.5 (Le Losq et al., 2014; Toplis et al., 1997). Similar patterns were also observed in (Giordano et al., 2006) in multicomponent silicate melts in a wide range of compositions.

The incorporation of iron in NAS subtly broadens the variability of the system's physical properties. Indeed, ferrous iron (Fe^{2+}) may act as a network modifier and charge balancer, while ferric iron (Fe^{3+}) can compensate as a network former, spanning from 4-, 5- and 6-fold coordination thus, playing different structural roles. Moreover, low-*T* heat

* Corresponding author at: Department of Earth Science, University of Torino, I-10125 Torino, Italy.
E-mail address: michele.cassetta@unito.it (M. Cassetta).

https://doi.org/10.1016/j.chemgeo.2024.122561
Received 15 July 2024; Received in revised form 27 November 2024; Accepted 8 December 2024
Available online 10 December 2024

capacity, optical absorption, and low-*T* Mössbauer spectroscopy studies have highlighted the presence of isolated Fe^{3+} ions, as well as Fe^{3+}–O^{2+}– Fe^{3+} and Fe^{3+}–O^{2+}– Fe^{2+} interactions. These interactions form iron-bearing clusters in soda-lime silicate and natural volcanic glasses, underscoring the iron's complex structural contributions (Bingham et al., 1999; Szewczyk and Cassetta, 2024).

To resume: (*i*) iron is the only major element of silicate melts occurring across multiple oxidation states at the same time which are (at atmospheric conditions) chemical-dependent; (*ii*) depending on the composition of the glass, the coordination of Fe^{3+} ions is either fourfold, fivefold or sixfold (Mysen, 2006) and (*iii*) if there is a concentration of mono- and divalent- cations greater than that of Fe^{3+} all Fe^{3+} switches to 4-fold coordination to balance the excess charge of the tetrahedra (T = Si^{4+}, Al^{3+} or Fe^{3+} coordinating cation). Electron spin resonance (ESR) study in binary silica-alkali/alkaline earth systems revealed that Fe^{2+} ions are primarily octahedrally coordinated, with an increase of the tetrahedral sites proportional to the alkali/alkaline earth ionic radius (r_i). Conversely, Fe^{3+} ions favor tetrahedral sites, proportionally to the alkali/alkaline earth r_i ratios. Thus, type and size of alkalis influence deeply the iron's site parameters across both redox states (Bingham et al., 2002). However, X-ray absorption near edge structure (XANES) and Mössbauer spectroscopies studies on similar compositions revealed a notable presence of octahedral Fe^{3+} (Antoni et al., 2004; Zimova and Webb, 2006). In peraluminous melts (*i.e.* melts with an excess of aluminum with respect to the alkali), the competition between Al^{3+} and Fe^{3+} for charge compensation, will favor the suppression of Fe^{3+} to promote Fe^{2+} (Cicconi et al., 2020; Le Losq et al., 2019), while for peralkaline melts (those for which there is an excess of alkali compensating cations) Fe^{3+} is favoured compared to Fe^{2+}. Therefore, the redox ratio of iron (Fe^{3+}/Fe_{tot}) in silicate glasses increases with the total iron content and in particular, in meta-aluminosilicate glasses, this ratio depends strongly on the electronic properties of the cation balancing Al^{3+} in tetrahedral coordination (Mysen, 2006). However, the way iron affects the macroscopic properties of glasses seems likely non-linear and sometimes uncorrelated. For instance, compared to Fe^{2+}, Fe^{3+} is more rigidly bonded within the glass network (Holland et al., 1999) suggesting an increase of the T_g correlated to the total iron oxide ($FeO_{tot.}$) quantity (which is likely linked to an increasing elastic performance of the medium) although when compared to Na_2O, Al_2O_3 and SiO_2 variations, the behavior turns out strongly non-linear. Indeed, also T_g correlates non-monotonically with the FeO_{tot} content in doped binary soda-silica glasses (Belova et al., 2015), therefore, it suggests a sort of tipping point above which, any relation between the structural and physicochemical property of the material is lost. In the present work we delve into the role of FeO_{tot} in comparison to aluminum, examining how it: (*i*) modifies the structure; (*ii*) balances the charge; and (*iii*) affects the thermal properties of the glass. Finally, we discuss the potential implications of our findings, extending the analysis to more complex natural and industrial materials and processes.

2. Methods

2.1. Glass synthesis

Six glasses, containing an FeO_{tot} load from 0 to 13.9 wt%, were synthesized by melting pure-grade powder reagents (SiO_2-Al_2O_3-Fe_2O_3-Na_2CO_3) in Pt crucibles in a muffle furnace at 1870 K for 2 h at the University of Trento. The melts were then poured in a copper plate and quenched in air.

2.2. Chemical composition and density

The chemical composition of the glasses (Table 1) was determined at the Institute of Earth System Sciences, Leibniz University Hannover using a JEOL JXA-iHP200F Field Emission Electron Probe Microanalyzer. Beam conditions on unknowns and calibration standards were

Table 1
Chemical composition in wt%, Fe/(Fe + Al) molar index, density (ρ) at room temperature, the atomic packing density C_g calculated with eq. 1, (Rouxel, 2007) and the two glass transition temperatures (T_g) obtained *via* dilatometry and DSC with a heating rate of 10 K min^{-1}.

	NAS 1	NASF 2	NASF 3	NASF 4	NASF 5	NASF 6
SiO_2	76.6	73.8	72.0	71.0	68.2	66.3
Al_2O_3	3.2	3.2	3.2	3.3	3.2	2.7
FeO_{tot}	–	2.2	4.4	6.4	8.2	13.9
Na_2O	19.6	19.7	19.1	19.0	19.0	16.9
Fe/(Fe + Al)	–	0.50	0.66	0.73	0.78	0.92
ρ [g cm^{-3}]	2.41	2.45	2.47	2.50	2.52	2.60
C_g	0.488	0.491	0.491	0.492	0.493	0.498
$T_{g,DIL}$ [K]	749.6	744.7	742.5	740.6	739.5	750.6
$T_{g,DSC}$ [K]	751.8	745.2	745.2	743.3	739.3	751.1

15 kV and 8 nA and defocused to 30 μm spot size. At these conditions, well-known sodium (Na) loss was not observed within 10 s (it was checked by measurements of Na counts each 200 msec per 1 min). Then, crystals were used to acquire peak and background positions: PETL for Si (Kα), TAPL for Al (Kα), TAPH for Na (Kα) and LIFH for Fe (Kα). Measurement peak and background time were 10 and 5 s, respectively, for Si, Al, and Fe, and 5 and 2 s, respectively, for Na. Elements calibration was carried out using in-house basaltic glass standards whose compositions were verified against certified MPI-DING reference glasses (Jochum et al., 2006). Two additional in-house Na_2O-rich albite and jadeite glasses were used as unknown references.

The density of the glassy compounds was measured using an Ultrapyc5000 He-pycnometer from Anton Paar®. All values reported in Table 1 represent the average of 99 runs, performed at 20 °C in pulse mode (10 pulses) at the pressure of 10 psi.

2.3. Mössbauer spectroscopy

Room temperature Mössbauer spectroscopy (MS) was performed at the Department of Chemical Science, University of Padova, using a constant acceleration spectrometer mounting a room-temperature Rh matrix ^{57}Co source, nominal strength 1850 MBq. The spectra were collected by dispersing ~80 mg of grinded powder in petroleum jelly. The obtained spectra were fitted to Lorentzian line shapes using a minimum number of sextets and doublets. Every attempt to fit the spectra using a Gaussian QSD model according to Voight-based methods (Rancourt and Ping, 1991) failed to yield satisfactory results. The obtained hyperfine parameters, isomer shift (δ), quadrupole splitting (Δ) or quadrupole shift, half linewidth at half maximum (Γ_+), are expressed in mm s^{-1}, while the relative areas (A) in %. The velocity was calibrated against a a-Fe foil and d is quoted relative to metallic Fe at room temperature. Recoilless fractions *f* for Fe^{2+} and Fe^{3+} were considered equal (Lalonde et al., 1998). This approximation was considered acceptable taking in to account that the instrumental error is presumed to be greater than the error incurred by evaluating the areas without considering different *f* values.

2.4. Thermal analysis

A simultaneous thermogravimetric and differential scanning calorimetry (DSC) analyzer (TGA-DSC 3+, Mettler Toledo) was used to carry out thermally analyze the materials as described in (Cassetta et al., 2023a). To remove the thermal history of the sample, a polished glass chip (about 10 mg) was placed in an alumina crucible and heated from 300 to 850 K at 20 K min^{-1} under air flowing at a rate of 100 mL min^{-1}. After cooling to ambient temperature at a rate of 10 K min^{-1}, the temperature was raised at the same rate up to 850 K, until a relaxed state was reached at the liquidus temperature. Analogously, a second approach to cross-validate the T_g was carried out by dilatometric (DIL) tests with a Linseis L75 horizontal dilatometer, equipped with an

alumina tube and piston. The tests were performed on glass fragments measuring 16–19 mm in length and with a cross-sectional area between 10 and 20 mm^2. The measurements were performed in a static air atmosphere with the same heating-cooling-heating path used for the DSC. The actual sample temperature was recorded using an S-type thermocouple in contact with the sample surface. A load of 250 mN was applied by the dilatometer piston onto the samples. T_g were subsequently determined (for both approaches) at the onset of the glass transition through the tangents line method, such as the point where the tangent to the heat flow curve in the glassy state and that to the inflection point in the glass transition interval cross (as shown in Fig. 1 a and b).

2.5. Vibrational dynamics

The vibrational dynamics was investigated by Raman, attenuated total reflectance (ATR) and Fourier transform infrared (FTIR) spectroscopies. The Raman spectral range was investigated by two spectrometers. (*i*) Between 200 and 1300 cm^{-1} unpolarized Raman spectra were obtained by a Thermo Scientific DXR2, equipped with solid-state laser having an emission wavelength λ_{exc} at 532 nm and with a proper edge filter for the Rayleigh line cut-off. The scattered radiation was dispersed by a high-resolution grating (1800 grooves) and detected by a charge-coupled device that was thermo-electrically cooled while the average spectral resolution was 2.9 cm^{-1}. (*ii*) Below 200 cm^{-1}, measurements were carried out in crossed polarization (HV) by using a Horiba-Jobin Yvon T-64000 triple-axis spectrometer in a double subtractive configuration, equipped with three holographic gratings (1800 lines/mm) and in back-scattering geometry. The spectrometer featured a charge-coupled device (CCD) detector (1024 × 256 pixels) cooled by liquid nitrogen, providing a spectral resolution of approximately 0.6 cm^{-1} per pixel. The laser source consists on a solid-state laser Cobolt Fandango 04-DPL with a λ_{exc} at 514.4 nm, 50 mW while the laser power at the sample surface was set at 10 mW.

ATR-IR and FTIR spectra were recorded between 400 and 1500 cm^{-1} by means of ThermoFisher Nicolet iS50 comprising an ATR accessory (Thermo Fisher) equipped with Nicolet Omnic 9.13.1224 software at a spectral resolution of 4 cm^{-1} with 100 and 48 scans for each acquisition, respectively. FTIR spectra were acquired on KBr pellets obtained by pressing a homogenized mixture of grinded glass sample and dried infrared grade KBr powder in a weight ratio of 1:100, respectively. The spectrum of a pure KBr tablet was used for the background correction.

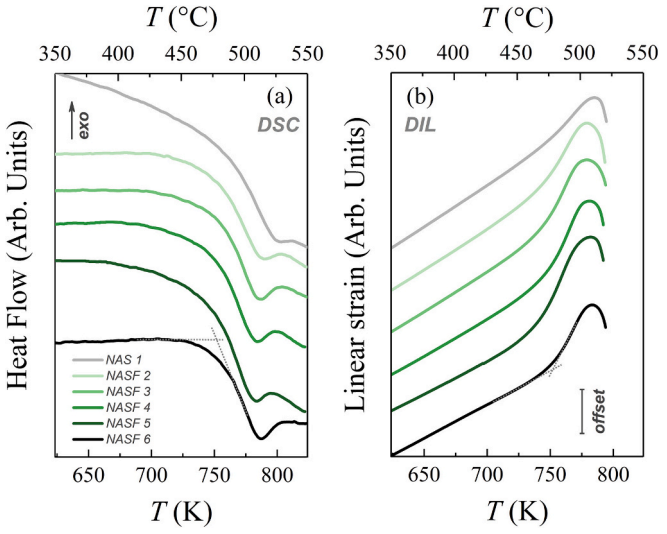

Fig. 1. Heat flow as a function of temperature obtained by DSC (a) and linear strain as a function of temperature obtained by dilatometric analysis (b). Measurements were carried out across the glass transition with a heating rate of 10 K min^{-1}. The samples were previously heated and cooled at 10 K min^{-1}.

3. Results

The FeO_{tot} load varies between 0 and 13.9 wt% while keeping the ratio constant amongst the other oxides (SiO_2, Al_2O_3 and Na_2O, see Table 1). The density of the system linearly increases from 2.41 g cm^{-3} (Fe-free NAS sample) to 2.60 g cm^{-3} (FeO_{tot} = 13.9 wt%). Fig. 1 (a) reports the heat flow measured by DSC as a function of temperature, whilst Fig. 1 (b) shows the linear strain (*i.e.* the fractional length variation of the investigated specimens) against temperature measured by dilatometry for the analyzed Fe-bearing glasses.

The T_g values measured by DSC and dilatometry, differing each other of at maximum 2.8 °C, decrease as FeO_{tot} increases from 0 to 8.2 wt%, from ~750 to 739 K (Table 1). The sample NASF 6 (FeO_{tot} = 13.9 wt%) shows an increase of the T_g to about 751 K.

Regarding Mössbauer spectra (in Fig. 2), the best fitting was obtained by using the minimum number of doublets for each sample. All spectra show an intense absorption near zero velocity, due to Fe^{3+} nuclei, together with a weaker ones, centered at ~2 mm s^{-1}, due to the high velocity component of the Fe^{2+} absorption. In general, a unique model was not relevant for all the spectra. For instance, sample NASF 3 and NASF 4 were properly fitted by using two doublets whose parameters, reported in Table 2, are ascribable to Fe^{3+} and Fe^{2+} species in distorted octahedral environments. Sample NASF 5, similarly to previous sample, shows a single Fe^{3+} distorted octahedral site and two different Fe^{2+} sites. These are representative of distorted octahedral (δ: 1.05 mm s^{-1}, Δ: 2.3 mm s^{-1}) and tetrahedral (δ: 1.03 mm s^{-1}, Δ: 1.72 mm s^{-1}) sites. Conversely, sample NASF 6 shows the presence of two different Fe^{3+} sites: the former exhibit hyperfine parameters correlated to distorted octahedral environment (δ: 0.41 mm s^{-1}, Δ: 0.85 mm s^{-1}), while the latter to distorted tetra-coordinate or penta-coordinate (δ: 0.20 mm s^{-1}, Δ: 0.85 mm s^{-1}) ferric nuclei. The ferrous population is distributed, similarly to sample NASF 5, over two sites: a distorted octahedral one (δ: 1.05 mm s^{-1}, Δ: 2.25 mm s^{-1}) and a distorted tetrahedral (δ: 1.02 mm s^{-1}, Δ: 1.7 mm s^{-1}) one.

All samples are characterized by a broad linewidth in each doublet: this evidence is significant of species distributed in a glassy matrix.

Table 1 reports also the atomic packing density (C_g) calculated after having estimated the Fe^{2+}/Fe_{tot} and recalculated the FeO and Fe_2O_3, according to (Rouxel, 2007):

$$C_g = \rho \frac{\sum f_i V_i}{\sum f_i M_i} \quad (1)$$

Where for the *i*th element in the form A_xB_y we have: $V_i = 4/3\pi N (xr_A^3 + yr_B^3)$, ρ being the density, N the Avogadro number, r_A and r_B are the ionic radii, f_i is the molar fraction and M_i the molar mass.

Fig. 3a shows that the region of the Raman spectra between 250 and 600 cm^{-1} encompasses the typical ring vibrations bands that could be divided in three sub-set: *i*) the first region (250–500 cm^{-1}), dominated by the 5- and 6-membered (or even higher) rings (the so-called R) and chain-like rings (R_c band (Hehlen et al., 2017)); *ii*) a shorter wavenumber interval 500–550 cm^{-1} governed by 4-membered rings (D_1 band) and *iii*) 3-membered rings (D_2 band) at about 600 cm^{-1} (Galeener, 1979; Hehlen et al., 2017; Matson et al., 1983; McMillan and Piriou, 1983). As $FeO_{tot.}$ content increases the R band develops a pronounced shoulder starting from 4.4 wt% (NASF 3) while the D_1 band seems much hybridized with the so-called R_c band of the binary Na_2O-SiO_2 systems and shift towards higher frequencies sharpens. The D_2 band (around 600 cm^{-1}) band does not show an evident frame in this system, but it is possible to observe as a shoulder in NAS 1 to disappears (or experiencing a drastic weakening) in NASF 6, carrying 13.9 wt% of FeO_{tot}. This suggests that the increasing content of FeO_{tot} promotes the formation of large rings (mirrored by the increasing-widening of the R band), accompanied by a decrease (or a topological modification) of the 4-membered rings (as revealed by the D_1 behavior) while the number of 3-membered rings seems also gently decreasing at least about 13.9 wt%

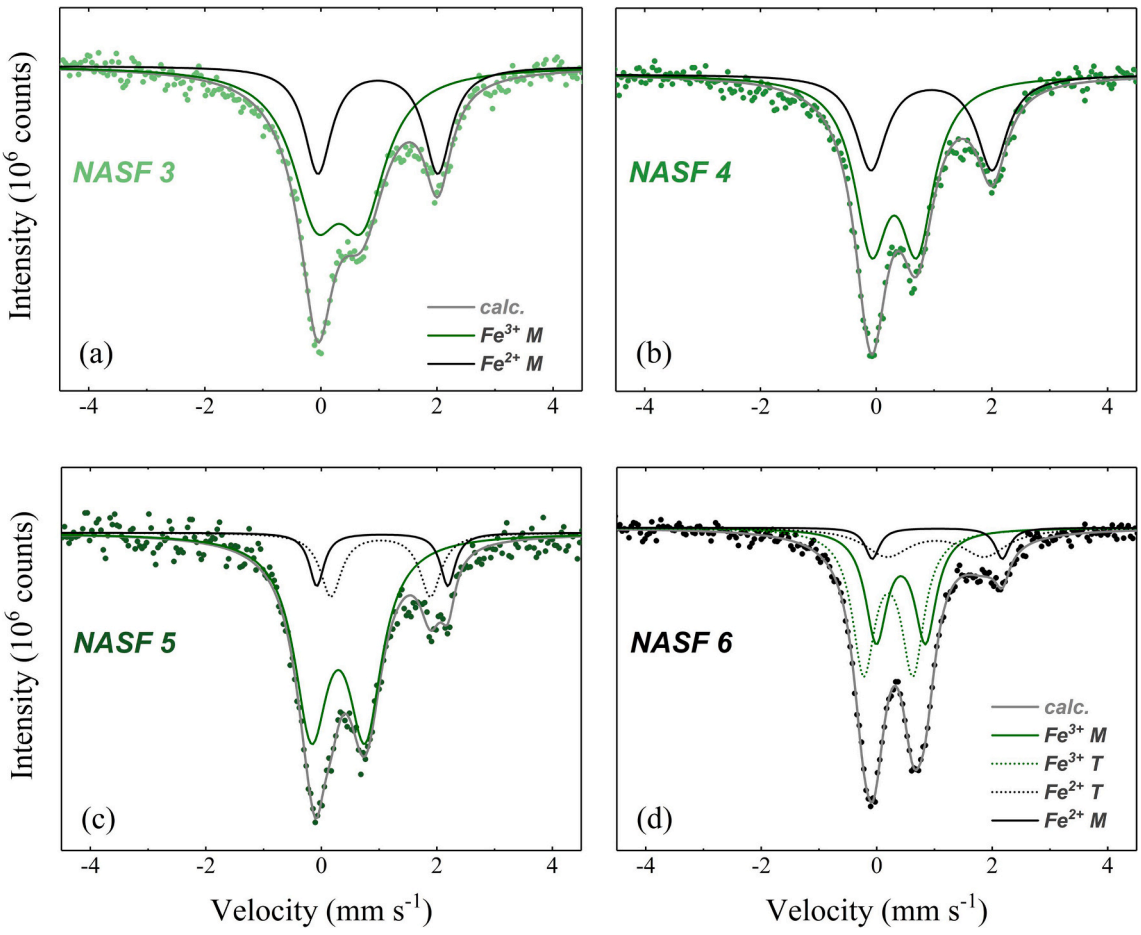

Fig. 2. Mössbauer spectra of four peralkaline glasses. Solid and dashed green lines represent the fitting of the Fe^{3+} octahedrally (M) and tetrahedrally (T) coordinated while solid and dashed black lines represents those of Fe^{2+}. (For interpretation of the references to colour in this figure legend, the reader is referred to the web version of this article.)

Table 2
Mössbauer results, (δ) isomer shift, (Δ) quadrupole splitting, (Γ) full width at half band maximum expressed in mm s^{-1}.

Sample	δ (mm s^{-1})	Δ (mm s^{-1})	Γ_+ (mm s^{-1})	A (%)	Fe^{2+}/Fe^{3+}	Fe^{3+}/Fe_{tot}	Attribution
NASF 3	0.31 (3)	0.79 (7)	0.49 (5)	68 (3)	0.47 (4)	0.68	Fe^{3+} **M**
	0.98 (3)	2.06 (6)	0.28 (3)	32 (2)			Fe^{2+} **M**
NASF 4	0.31 (3)	0.79 (7)	0.35 (2)	65 (3)	0.53 (4)	0.65	Fe^{3+} **M**
	0.90 (10)	2.10 (2)	0.31 (4)	35 (2)			Fe^{2+} **M**
NASF 5	0.29 (1)	0.93 (4)	0.35 (2)	75 (4)	0.33 (3)	0.75	Fe^{3+} **M**
	1.03 (3)	1.72 (8)	0.22 (2)	16 (1)			Fe^{2+} **T**
	1.05 (2)	2.30 (10)	0.16 (8)	9 (2)			Fe^{2+} **M**
NASF 6	0.41 (9)	0.85 (2)	0.22 (4)	33 (2)	0.29 (3)	0.77	Fe^{3+} **M**
	0.20 (7)	0.85 (3)	0.26 (5)	44 (2)			Fe^{3+} **T**
	1.02 (9)	1.70 (5)	0.47 (9)	17 (2)			Fe^{2+} **T**
	1.05 (6)	2.25 (9)	0.20 (1)	6 (1)			Fe^{2+} **M**

of FeO_{tot}.

The peak position of the 700–850 cm^{-1} band (originated by the T–O stretching vibrations along the T–O–T plane (Kalampounias et al., 2006)) weakens and appears to shift to slightly higher values as iron increases from NAS 1 to NASF 6.

The interval of the short-range order in the Raman spectra between 850 and 1250 cm^{-1} varies notably with FeO_{tot} in the glass. It is important to observe that, there is a significant variation in intensity at 960 cm^{-1} with FeO_{tot}. This band belongs to the Fe^{3+} asymmetric stretching vibrations (Cassetta et al., 2023a; Di Genova et al., 2017; González-García et al., 2020; Le Losq et al., 2019). Although its assignation is still a matter of debate, its shape and intensity are also affected by the contribution of iron to both two- and three-bridging oxygen configurations per tetrahedron, denoted as Q^2 and Q^3, respectively (Cassetta et al., 2024; Cassetta et al., 2023c). However, it can be considered (at least the intensity measured at a fixed frequency) as a fingerprint of Fe^{3+} regardless of its coordination (Le Losq et al., 2021). Table 3 shows the normalized intensity of the antisymmetric stretching of the Fe^{3+} band (taken at 960 cm^{-1}) and that of the Q^3 (taken at 1090 cm^{-1}) pointing out how the change of their normalized intensity is correlated to the increasing $FeO_{tot.}$ content, through the increasing of Fe^{3+}–O–Si complexes. The iron contribution in replacement of Q^3 provided by Al^{3+} can be indicated by the ratio (R#) between Q^3 and Fe^{3+} that increases from 0.3 (NASF 2) to 2.1 (NASF 6).

ATR-IR and FTIR spectra reported in Fig. 3(b-c), show three main bands, with minima at around 460 cm^{-1}, 770 cm^{-1} and 1000 cm^{-1}. The characteristic silicate glass signatures are ascribed to asymmetric bending (a-φ) vibrations of the T–O–T bonds of coordinated Si in the

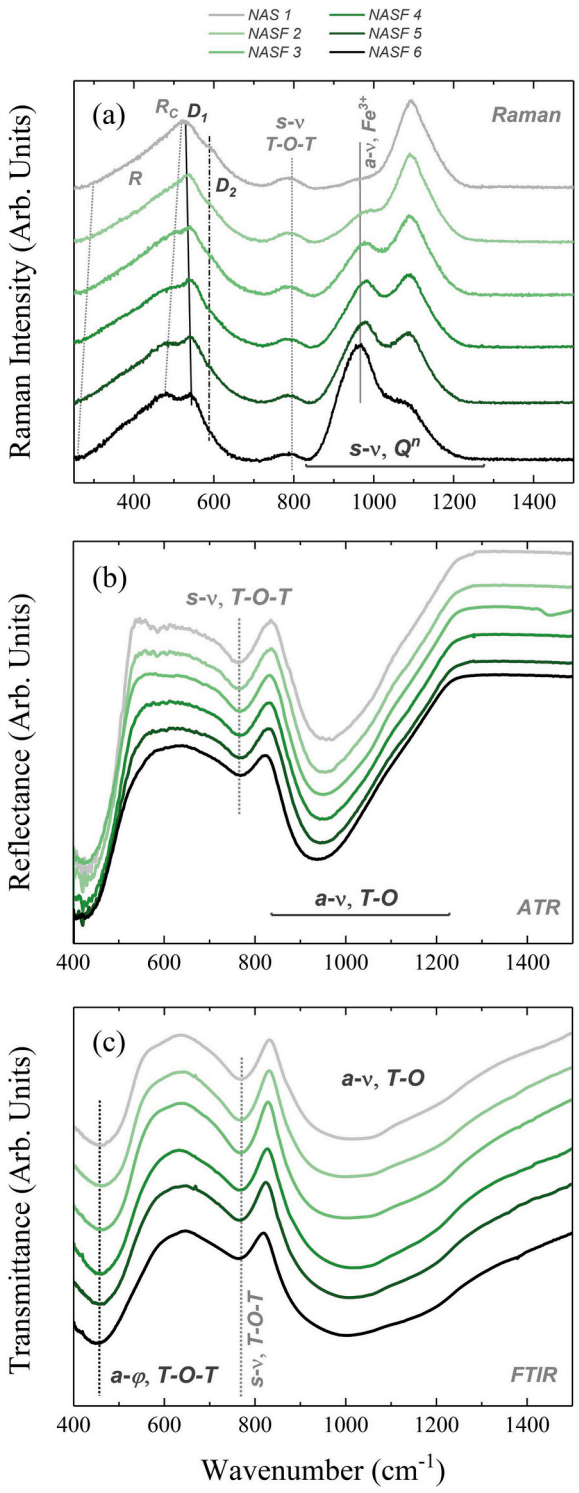

Fig. 3. Raman (a), ATR-IR (b) and FTIR (c) spectra of the Fe-bearing peralkaline soda aluminosilicate glasses. Lines corresponds to the assignation reported in Table 3 and 4.

Table 3
Normalized intensity to that of the s-ν of Q^3 measured at 1090 cm^{-1} and that of Fe^{3+} a-ν stretching measured at 960 cm^{-1}.

	NASF 2	NASF 3	NASF 4	NASF 5	NASF 6
(a-ν),Fe^{3+}	0.32	0.61	0.84	0.94	1
(s-ν),Q^3	1	1	1	0.85	0.47
R#	0.32	0.61	0.84	1.10	2.10

tetrahedron structure of SiO_4 (Agarwal et al., 1995; Hemmati and Angell, 1997; Ritz, 2023), symmetric stretching (s-ν) of T-O-T bridges and asymmetric stretching (a-ν) vibrations of T–O, (Dalby and King, 2006) (see Table 4 for the assignments and observed wavenumbers). The peak width of the band associated with the s-ν of the tetrahedron structure of Si^{4+}, Al^{3+} and Fe^{3+} becomes wider and shifts towards lower frequencies with increasing amount of FeO_{tot} (from grey to dark-green) indicating a modification of the tetrahedron structure which can be due to the increased substitution of Si^{4+}, Fe^{3+} and Al^{3+}. This effect is much more pronounced and appreciable in the ATR-IR spectra, suggesting that the ATR seems to be more sensible to such kind of chemical variations. Moreover, a gradual shift towards lower wave numbers can also be found for the band centered around 460 cm^{-1} and for the one at 1100 cm^{-1} which can be attributed to the increasing presence of the iron content resulting in the elongation of the T–O bond and in a consequent reduction of the bond angle (Dalby and King, 2006).

Overall, as reported for a similar system in (Tasheva et al., 2023), two effects on the spectra can be attributed to the increasing presence of iron in the glasses which results in a modification of the structure of the glass: a gradual shift of the main bands to lower wavenumbers and both a broadening and intensification of such bands.

The three complementary spectroscopic techniques unanimously highlight "an expected" structural broadening that correlates with a decreasing glass transition temperature until a certain concentration threshold is reached (between 8.2 and 13.9 wt%).

The analysis of low-frequency Raman spectra, Fig. 4 (a), was carried out following the protocol (Shuker and Gammon, 1970) and by considering the observed intensity (I^{obs}), proportional to the density of states $g(\omega)$. For a Stokes process the I^{obs} frequency-dependence can be written as:

$$I^{obs}(\omega) = C(\omega)g(\omega)\frac{[n(\omega T)+1]}{\omega} \quad (2)$$

Here $C(\omega)$ is the light to vibration coupling function and is considered $\sim \omega$ in the Boson Peak (BP) range. Dividing $I^{obs}(\omega)$ by $[n(\omega,T)+1]$ (where $n(\omega,T)$ is the Bose-Einstein factor) and frequency (ω), the reduced Raman intensity $I^{red}(\omega)$ is obtained:

$$I^{red}(\omega) = C(\omega)\frac{g(\omega)}{\omega^2} \quad (3)$$

The BP frames was analyzed according to the log-normal distribution according to (Malinovsky et al., 1991). Therefore, the BP position shifts of ~5 cm^{-1}, only slightly from NAS to NASF 6 (from ~57.3 cm^{-1} to ~62.5 cm^{-1} respectively) while its maximum becomes more and more suppressed showing an intensity reduction (I^{red}) of ~60 % from NASF 6 to NAS 1, see Fig. 3 (a). The results align with the literature, as the NAS 1 sample, which has a composition similar to the binary NS 25 glass (Cassetta et al., 2023b), exhibits comparable behavior, while the BP intensity trend matches that reported for unpolarized Raman spectra in (Antonio et al., 2024), where the BP intensifies as the iron content increases. The reduced spectra $I^{red}(\nu)$ was further examined by considering

Table 4
ATR and FTIR band assignments in terms of vibrational modes (bending = φ, stretching = ν, a = antisymmetric and s = symmetric) and observed wavenumbers.

	NAS 1	NASF 2	NASF 3	NASF 4	NASF 5	NASF 6
ATR	Wavenumber (cm^{-1})					
s-ν	764.6	768.5	768.0	765.1	764.6	768.0
a-ν	957.5	954.1	950.7	942.6	945.4	935.3
FTIR	Wavenumber (cm^{-1})					
a-φ	459.9	463.8	463.8	460.4	459.9	452.2
s-ν	768.5	768.5	768.5	768.5	765.1	764.7
a-ν	1011.5	996.1	1000.4	1015.4	1011.5	1004.3

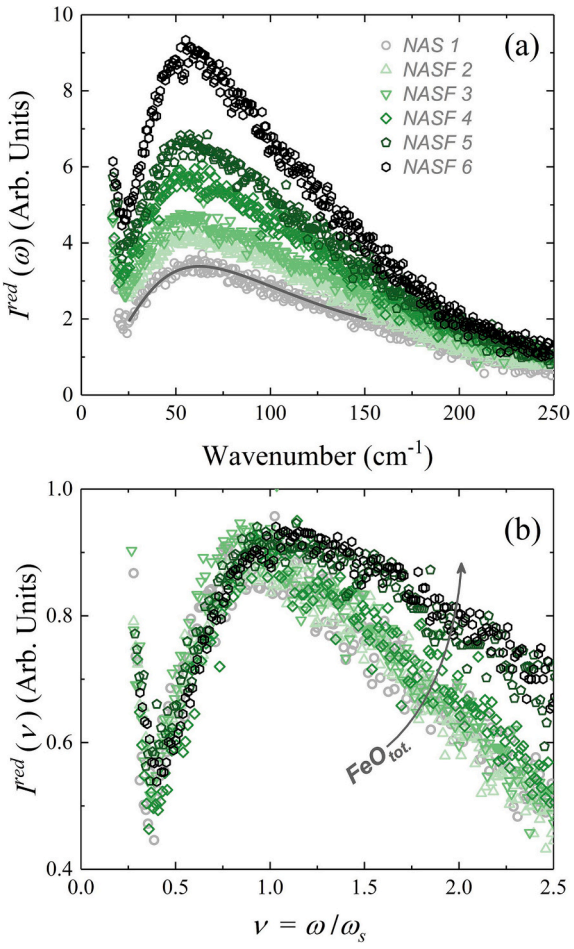

Fig. 4. (a) Reduced intensity of the HV Raman spectra in the low-ω region. (b) Results of the scaling procedure of the BP. Grey arrow marks the direction of the increasing FeO_{tot} content.

the reduced-squeezed frequency $\nu = \omega/\omega_S$ as defined in (Cassetta et al., 2022; Zanatta et al., 2010), and by transforming the variable as $g(\nu)d\nu = g(\omega)d\omega$. Here, the parameter ω_S is called squeezing frequency and is defined as the frequency at which all the spectra are expected to lies in the same master curve at the same $I^{red}(\nu)$ value with the following formula:

$$I^{red}(\nu) = I^{red}(\omega)\ \omega_S^2 \tag{4}$$

The results are reported in Fig. 4 (b) and BP spectra show a nice scaling amongst the Fe-free glass (NAS 1) and samples loaded with up to 6.39 wt% (NASF 4). Then, for higher iron content the scaling drops and apparently provides a second master curve shaped by NASF 5 and NASF 6 (loaded with 8.2 and 13.9 wt% of $FeO_{tot.}$ respectively). Notably, the higher frequency tail of the BP follows the same kind of scaling-drop observed in (Cassetta, 2024; Cassetta et al., 2023a), this being probably due to a deviation of the Fe-contributing network towards a dominant 4-fold coordination.

4. Discussion

The combined DSC, dilatometry, Raman, IR and Mössbauer spectroscopy technique results revealed that the sample response is influenced by the iron content, and, in particular, by its oxidation state. Specifically, it can be observed a parallel interplay between Fe^{2+} and Fe^{3+} in which: (*i*) the local environment becomes more and more tetrahedrally coordinated as the Fe^{3+} increases and (*ii*) the replacement of the peralkaline-silicate component (SiO_2, Na_2O and Al_2O_3) with FeO_{tot} diminishes the T_g values until a certain limit, above which T_g rises again.

In order to examine the dissolution of Fe in the considered peralkaline compositions the variation of Fe^{3+}/Fe_{tot} in function of Fe/(Fe + Al) was plotted in Fig. 5 (a) and compared to data of (Mysen, 2006) on a jadeitic metaluminous silicate composition ($NaAlSi_2O_6$), to which a variable amount of FeO_{tot} ranging from 0.9 to 5.6 mol% was added.

Using the well-known correlation between Fe^{3+}/Fe_{tot} and the a-ν Fe^{3+} band in Raman scattering (Di Genova et al., 2016; Le Losq et al., 2021), we extrapolated the relationship between the intensities of the a-ν Fe^{3+} Raman bands (Table 3) and the Fe^{3+}/Fe_{tot} ratio obtained *via* Mössbauer spectroscopy (Table 2). It was found that in our system the two parameters follow the relation $Fe^{3+}/Fe_{tot} = 0.2314(\text{a-}\nu),Fe^{3+} + 0.5164$ that was following exploited to estimate oxidation state of the NASF 2 sample (green empty diamond in Fig. 5a).

The results show that Fe^{3+}/Fe_{tot} increases with the Fe_{tot} content and in (Mysen, 2006) was concluded that it decreases with the ionization potential of the charge-balancing cation. Here we observe indeed a very similar behavior probably related to: (*i*) the coordination number of Fe^{3+} changes from 4 to 6 as Fe^{3+}/Fe_{tot} decreases, with less distorted Fe^{3+}-O polyhedra at higher Fe^{3+}/Fe_{tot}; (*ii*) Fe^{2+} also exists in 4- to 6-fold coordination states. Our plot (green symbols) looks identical but shifted towards higher values of Fe/(Fe + Al) index, suggesting a similar chemical evolution. Fig. 5 (b) shows the relationship between the $T_{g,DSC}$, and the squeezing frequency ω_S, which describes the continuity of the elastic medium based on the scaling procedure, see eq. (3). We also

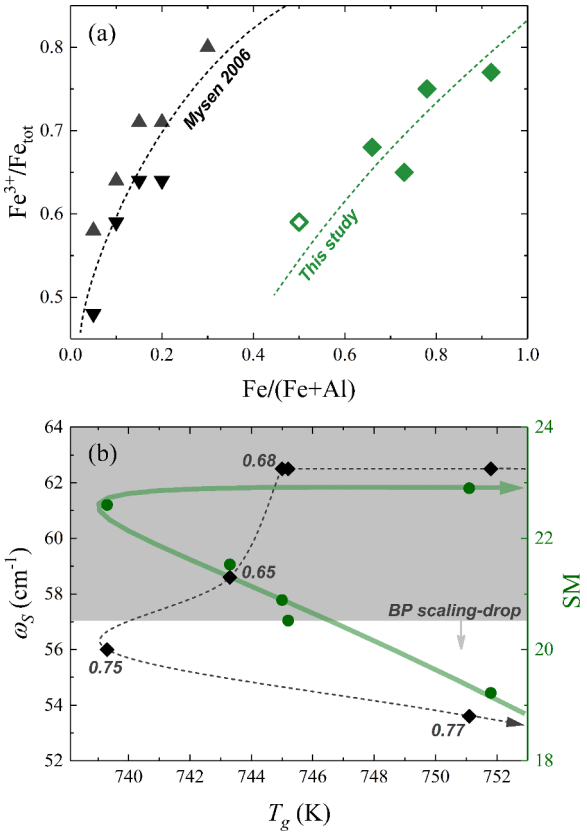

Fig. 5. Fe^{3+}/Fe_{tot} ratio measured by Mössbauer (green solid diamonds) and Raman-derive (green empty diamond) *versus* Fe/(Fe + Al) index compared to that reported by Mysen (Mysen, 2006) (black symbols), lines are guide for the eye (a). In (b) is reported the squeezing frequency ω_S (black diamonds, black axes) and SM (green dots, green axes) *vs.* T_g measured by DSC. The lines are guides for the eye, while the grey area represents approximatively the validity of the scaling procedure of the BP according to eq. (3). Labels report the Fe^{3+}/Fe_{tot}. (For interpretation of the references to colour in this figure legend, the reader is referred to the web version of this article.)

considered the role of the network structure modifier content, described by the empirical index (SM) calculated according (Giordano and Dingwell, 2003) as SM = $\Sigma(Na_2O + FeO_{tot}/2)$, calculated in mol %.

As T_g value decreases from approximately 752 K to 740 K, ω_S exhibits a non-linear trend. Initially, ω_S keeps the same value of its BP, then decreases and drops dramatically at the higher T_g. The SM demonstrates a relatively stable negative trend as T_g increases and a slight increase as T_g grows back at around 750 K. Thus, the parameter ω_S indicates the continuity of the elastic medium while its non-linear behavior with T_g suggests that the elastic properties of the glass significantly affect the heat capacity and entropy. The SM parameter, which includes the modifier oxides and $FeO_{tot}/2$, represents, therefore, a parameter descriptive of, the structure of the glasses analyzed here at first approximation. The slight increase in SM with T_g aligns with the idea that larger modifier content generally disrupts the network, potentially lowering T_g. The ratio of Fe^{3+}/Fe_{tot} plays a significant role in these trends. Lower ratios (*i.e.*, 0.65) correspond to a 1:1 scaling of BP, this meaning a conservation of similar distribution of the elastic properties; conversely, higher ratios (*i.e.*, 0.77) correspond to lower ω_S values and higher T_g this being related to larger Fe-content; Fe^{3+} is accountable not only to a change and redistribution of the elastic constants but also to a variation of the thermal properties.

The gradual increase in density from NAS 1 to NASF 6 (~7 %) is the result of the interplay amongst atomic weight, packing efficiency and atomic arrangement within the glass network. This results in an increase of the atomic packing density C_g only of ~4 % that is surely due to the extent of the degree of network connectivity, defined by the number of bridging oxygen atoms linking adjacent tetrahedral units. Nevertheless, the network connectivity (or polymerization degree) is tightly related to the coordination environment of cations that is in turn chemical dependent thus, it can exert a notable influence on the C_g. Generally, Fe^{3+}/Fe_{tot} is a positive function of the total FeO_{tot} content (Mysen et al., 1980). In particular, the isomer shift $\delta(Fe^{2+})$ expresses a transition from a single 6-fold coordinated ($^{VI}Fe^{2+}$) towards a coexistent 6- and 4-fold ($^{IV\text{-}VI}Fe^{2+}$) as the Fe^{3+}/Fe_{tot} increases along the series NAS 1 - NASF 6. Moreover, the evolution of $\delta(Fe^{2+})$, related to the Fe^{3+}/Fe_{tot}, suggests that the elevated Fe^{3+}/Fe_{tot} is correlated with lower coordination numbers of Fe^{2+} which seems quite aligned to what is concluded in (Farges et al., 2004; Mysen, 2006; Rossano et al., 2000) and with neutron diffraction and Mössbauer spectroscopy data from (Holland et al., 1999), thus revealing that the 4-fold coordination may exists for both Fe oxidation states.

Regarding the coordination of Fe^{3+} it shows a deviation towards a 4-fold coordinated system once the 8.2 wt% is exceeded (see Table 2). This behavior is quite commonly ascribed to the decreasing Fe^{3+}/Fe_{tot} as in (Mysen, 2006). However, the fitting results and shape of Mössbauer spectra, suggest the presence of distorted polyhedral site for the Fe^{3+}, highlighting the possibility of an average coordination, spanning from 6- to 4-fold and encompassing the distorted 5-fold coordination state (Alderman et al., 2017; Wilke et al., 2007). To summarize, the speciation and coordination of iron could directly influence the C_g, as different coordination states have distinct ionic radii (r_i) that may cause variations. To assess the magnitude of this effect, reasonably contextualized within the measurement uncertaint, we recalculated the C_g based on Mössbauer data and by following eq. 1, distributing the volumetric percentages according to the respective r_i of $^{IV}Fe^{3+}$, $^{VI}Fe^{3+}$, $^{IV}Fe^{2+}$, and $^{VI}Fe^{2+}$, which are 0.490, 0.645, 0.630, and 0.780 Å, respectively (Shannon, 1976). The newly calculated values do not differ significantly from those obtained using an average r_i for iron. However, when the system tends more towards the 4-fold state, the C_g values decrease only slightly (recalculated values are 0.492 and 0.496 for NASF 5 and 6 respectively).

The above considerations are directly related to the observed trend of the T_g. Indeed, the activation energy for viscous flow notably drops when $FeO_{tot.}$ substitutes Al_2O_3 (Mysen et al., 1985), explaining the decrease (although of 12.5 K) of the T_g, the peak of the glass transition interval as well as and the softening point. At the same time, the change at about 13.9 wt% of FeO_{tot} (sample NASF 6) is probably the harvest of a much more polymerized structure which could be considered equivalent to the Fe-free one (NAS 1). Generally, this trend agrees with that in (Antonio et al., 2024; Falenty and Webb, 2010), where the addition of iron systematically lowers the T_g. A possible explanation of this decreasing T_g is the lack of tetrahedrally coordinated trivalent atoms (Al^{3+} and Fe^{3+}) to charge balance the remaining mono and divalent atoms (Na^+ and Fe^{2+}), that may increase the configurational entropy of the system (the case of samples NAS 1 NASF 2–5). In particular, the results from Mössbauer spectroscopy indicate a substantial marginal role (or absence) of $^{IV}Fe^{2+}$ and $^{IV}Fe^{3+}$, (network former) which may keep constant or increases the T_g (Belova et al., 2015). This can be also seen through the abrupt intensity increase of the Raman a-ν Fe^{3+} band at about 970 cm^{-1} and the shift towards lower wavenumbers of the FTIR and ATR T-O-T antisymmetric stretching (a-ν band centroid. This structural evolution correlates to the changes of the R band, that widens with iron content mirroring an increasingly coordination of the T-membered rings (6-membered to higher units) as already reported in (Belova et al., 2015). Indeed, the splitting of the residual R_c band seems to suggest an evolution from chain-like structure towards a more homogeneous 3-D ring-network, wherein three-fold rings (observed at 600 cm^{-1} in NAS 1), possibly arranged in chains (Matson et al., 1983), are opened by divalent Fe^{2+} ions, breaking chains and form more 4-fold structures (see the emergence of the D_2 band), which are then redistributed homogeneously and three-dimensionally within the network. The progressive enrichment in iron and its decreasing coordination (from octahedral to predominantly tetrahedral), actively contributes to the formation of larger rings (6-fold and above). The possible coordination of iron in 5-fold (both Fe^{2+} and Fe^{3+}) could instead contribute both to deflecting the structure towards larger ring networks and to an increasing bonding strength with the same Fe^{3+} coordinated tetrahedra of the rings, explaining both the increase in T_g and the growing intensity of the BP. Indeed, being Fe^{3+} being more rigidly bounded within the network than Fe^{2+} due to shorter Fe—O bond, a densification-like of the vibrational states is induced that is observed through the strong BP at higher iron concentrations. The same effect is observed in (Cassetta et al., 2023a; Cassetta, 2024), where the BP shift towards lower wavenumbers and higher reduced intensities as Fe^{3+} content increases.

4.1. Implications

The oxidation state of iron may significantly affect silicate melt viscosity (Chevrel et al., 2013; Stabile et al., 2016; Zimova and Webb, 2006), impacting magma ascent and eruption explosivity. Fe^{2+} acts often as a network modifier, reducing viscosity, while Fe^{3+}, though traditionally considered a network former, behaves also like a modifier depending by the coordination (function of its chemical environment). Observations in eutectic andesitic and basaltic melts demonstrate that a reduction in the Fe^{3+}/Fe_{tot} ratio decreases viscosity (*i.e.* Fe^{3+}/Fe_{tot} from 0.6 to 0.2 in andesitic melts reduces viscosity by two orders of magnitude near T_g (Liebske et al., 2003), whereas basaltic melts show a ~ 1 log unit decrease for similar changes (Chevrel et al., 2013)) potentially triggering transitional behaviour duringeruption (Di Genova et al., 2017; Giordano et al., 2010; Stabile et al., 2016; Jones et al., 2022b; Jones et al., 2022a). These effects are amplified at undercooled temperatures, where structural disorder and configurational entropy dominate (Richet and Neuville, 1992). Indeed, viscosity changes in peralkaline magmas likely reduced discharge rates at volcanic vents, affecting the emplacement dynamics and highlighting melt composition's role in magmatic intrusions, see the case of Glass House Mountains (Webb, 2021) as well as effusive-explosive eruptions in Pantelleria island (Di Muro et al., 2009; Stabile et al., 2016; Neave, 2020). These chemical variations (based on low aluminum, *i.e.* down to 7 % in (Antonio et al., 2024; Webb, 2021)) becomes significantly more complex when involving iron in a system experiencing rapid redox fluctuations (*i.*

e. when magma nears the surface). This could occur even over surprisingly short timescales, making the prediction of the system's response complicated during magma ascent and eruptions (as well as during industrial processes (Antonio et al., 2024; Nodari et al., 2025)). Additionally, the rapid crystallization tendency of iron clusters (Szewczyk and Cassetta, 2024) for iron-based nanolite-bearing natural or industrial melts, subtracts FeO_{tot} from the melt, introducing a double-effect that thickens and toughens the material through a multipronged increases of the residual liquid (due to iron-depletion) and apparent viscosity (Cáceres et al., 2020; Cassetta et al., 2023c; Di Genova et al., 2020; Giordano et al., 2021; Hornby et al., 2024; Okumura et al., 2022).

Of particular interest here is that by considering our compositional shift caused by a scenario of "iron depletion upon magnetite crystallization", we observe clearly a non-linear relationship of T_g and vibrational densities of states, thus a non-direct view on elasticity. The increased viscosity, hardening, crystallization and bubbles nucleation drift, further accelerates this non-linear trend and the feedback loop intensifies the system's tendency to shift from effusive to explosive eruptive styles. In this process, small variations in iron content, oxidation and coordination can have a large impact on the melt's behavior, introducing a further level of unpredictability in volcanic eruption styles. The non-linear interactions between viscosity, gas content, and magma dynamics can complicate predictions of eruption intensities and their associated hazards.

5. Conclusion

The incorporation of iron into peralkaline silicate glasses significantly affects the structure, charge balance, and thermal properties. Iron alters the network connectivity by changing the coordination states of Fe^{2+} and Fe^{3+} from 6- to 4-fold. This leads to a more polymerized structure with tetrahedral larger rings. The Fe^{3+}/Fe_{tot} ratio impacts the charge distribution within the glass network. Higher Fe^{3+}/Fe_{tot} ratios correlate with lower Fe^{2+} coordination, affecting the overall structure. Here Iron generally lowers the glass transition temperature (T_g). Nevertheless, at higher concentrations, tetrahedrally coordinated Fe^{2+} and Fe^{3+} act as network formers, increasing T_g by enhancing network rigidity and bond strength. Here we report the existence of a sort of iron concentration's tipping point above which the short-range structures still evolve linearly with density. Conversely, the medium-range structure experiences a kind of re-enrichment of T units, deviating towards a different elastic medium described by the scaling-drop of the BP around 8.2 wt% which possibly explains the observed jump in the glass transition. Understanding how subtle changes in iron content, oxidation state, and coordination influence magma behavior is essential, as these variations introduce significant unpredictability to eruption styles. Consequently, the non-linear, iron-driven interactions between viscosity, gas content, and magma dynamics intensify the challenges of the doublet understanding-forecasting of the eruption intensity and associated hazards.

CRediT authorship contribution statement

Michele Cassetta: Writing – original draft, Visualization, Validation, Supervision, Methodology, Investigation, Formal analysis, Data curation, Conceptualization. **Emanuele De Bona:** Writing – review & editing, Methodology, Formal analysis, Data curation. **Alessia Sambugaro:** Writing – review & editing, Methodology, Investigation, Formal analysis, Data curation. **Francesco Enrichi:** Validation, Methodology, Investigation. **Nicola Daldosso:** Validation, Resources, Methodology, Investigation, Funding acquisition. **Beatrice Giannetta:** Writing – review & editing, Validation, Methodology, Formal analysis. **Claudio Zaccone:** Writing – review & editing, Validation, Resources, Methodology, Investigation, Formal analysis. **Mattia Biesuz:** Writing – review & editing, Validation, Resources, Methodology, Investigation, Funding acquisition. **Vincenzo M. Sglavo:** Writing – review & editing, Validation, Resources, Investigation. **Renat Almeev:** Writing – review & editing, Validation, Methodology, Formal analysis, Data curation. **Luca Nodari:** Writing – review & editing, Validation, Methodology, Investigation, Formal analysis, Data curation. **Daniele Giordano:** Writing – review & editing, Validation, Resources, Methodology, Investigation, Funding acquisition. **Gino Mariotto:** Writing – review & editing, Visualization, Validation, Resources, Funding acquisition.

Declaration of competing interest

The authors declare that they have no known competing financial interests or personal relationships that could have appeared to influence the work reported in this paper.

Acknowledgments

This work is dedicated to G. Salamina. M.C. and D.G. acknowledges support from PNRR M4C2 - PRIN 2022PXHTXM - STONE - A new generation Spectroscopy Tool to monitor rheology and phase transformation prOcesses in volcaNology and cEramic production funded by the European Union – Next Generation EU. R.A. was supported by the German Science Foundation (DFG Project AL1189/15).

Data availability

Data will be made available on request.

References

Agarwal, A., Davis, K.M., Tomozawa, M., 1995. A simple IR spectroscopic method for determining fictive temperature of silica glasses. J. Non-Cryst. Solids 185, 191–198. https://doi.org/10.1016/0022-3093(94)00676-8.

Alderman, O.L.G., Wilding, M.C., Tamalonis, A., Sendelbach, S., Heald, S.M., Benmore, C.J., Johnson, C.E., Johnson, J.A., Hah, H.Y., Weber, J.K.R., 2017. Iron K-edge X-ray absorption near-edge structure spectroscopy of aerodynamically levitated silicate melts and glasses. Chem. Geol. 453, 169–185. https://doi.org/10.1016/j.chemgeo.2017.01.020.

Antoni, E., Montagne, L., Daviero, S., Palavit, G., Bernard, J.L., Wattiaux, A., Vezin, H., 2004. Structural characterization of iron-alumino-silicate glasses. J. Non-Cryst. Solids 345–346, 66–69. https://doi.org/10.1016/j.jnoncrysol.2004.07.045.

Antonio, R., Bussey, J., Wilkins, M.C.J.D., Neuville, D., Cormier, L., McCloy, J., 2024. Effects of Al Substitution for Fe in $Na_5FeSi_4O_{12}$. Glas. Eur. 2, 151–164.

Belova, E.V., Kolyagin, Y.A., Uspenskaya, I.A., 2015. Structure and glass transition temperature of sodium-silicate glasses doped with iron. J. Non-Cryst. Solids 423–424, 50–57. https://doi.org/10.1016/j.jnoncrysol.2015.04.039.

Bingham, P.A., Parker, J.M., Searle, T., Williams, J.M., Fyles, K., 1999. Redox and clustering of iron in silicate glasses. J. Non-Cryst. Solids 253, 203–209. https://doi.org/10.1016/S0022-3093(99)00361-0.

Bingham, P.A., Parker, J.M., Searle, T., Williams, J.M., Smith, I., 2002. Novel structural behaviour of iron in alkali-alkaline-earth-silica glasses. Comptes Rendus Chim. 5, 787–796. https://doi.org/10.1016/S1631-0748(02)01444-3.

Cáceres, F., Wadsworth, F.B., Scheu, B., Colombier, M., Madonna, C., Cimarelli, C., Hess, K.-U., Kaliwoda, M., Ruthensteiner, B., Dingwell, D.B., 2020. Can nanolites enhance eruption explosivity? Geology XX 1–5. https://doi.org/10.1130/G47317.1/5074194/g47317.pdf.

Cassetta, M., 2024. Medium-range structure modifications induced by $Fe^{3+}/Fe_{tot.}$ In volcanic glasses: a low-frequency Raman spectroscopy study. Eur. Phys. J. Plus 139. https://doi.org/10.1140/epjp/s13360-023-04838-w.

Cassetta, M., Zanatta, M., Biesuz, M., Giarola, M., Mariotto, G., 2022. New insights about the role of Na–K ratio on the vibrational dynamics of synthetic-basalt glasses. J. Raman Spectrosc. 1–10. https://doi.org/10.1002/jrs.6298.

Cassetta, M., Giannetta, B., Enrichi, F., Zaccone, C., Mariotto, G., Giarola, M., Nodari, L., Zanatta, M., Daldosso, N., 2023a. Effect of the alkali vs iron ratio on glass transition temperature and vibrational properties of synthetic basalt-like glasses. Spectrochim. Acta - Part A Mol. Biomol. Spectrosc. 293, 122430. https://doi.org/10.1016/j.saa.2023.122430.

Cassetta, M., Mariotto, G., Daldosso, N., De Bona, E., Biesuz, M., Sorarù, G.D., Almeev, R., Zanatta, M., Vetere, F., 2023b. Viscosity, Boson Peak and Elastic Moduli in the Na_2O-SiO_2 System. Minerals 13, 1166. https://doi.org/10.3390/min13091166.

Cassetta, M., Vetere, F., Zanatta, M., Perugini, D., Alvaro, M., Giannetta, B., Zaccone, C., Daldosso, N., 2023c. Micro-Raman spectroscopy for a comprehensive understanding of the structural evolution of Basaltic-Andesite and Trachybasalt multiphase systems. Chem. Geol. 616, 121241. https://doi.org/10.1016/j.chemgeo.2022.121241.

Cassetta, M., Rossi, B., Mazzocato, S., Vetere, F., Iezzi, G., Pisello, A., Zanatta, M., Daldosso, N., Giarola, M., Mariotto, G., 2024. Deep-UV Raman spectroscopy: a novel

heuristic method to characterize volcanologically relevant glasses on Mars. Chem. Geol. 644, 121867. https://doi.org/10.1016/j.chemgeo.2023.121867.
Chevrel, M.O., Giordano, D., Potuzak, M., Courtial, P., Dingwell, D.B., 2013. Physical properties of $CaAl_2Si_2O_8$-$CaMgSi_2O_6$-FeO-Fe_2O_3 melts: Analogues for extra-terrestrial basalt. Chem. Geol. 346, 93–105. https://doi.org/10.1016/j.chemgeo.2012.09.004.
Chinnam, R.K., Francis, A.A., Will, J., Bernardo, E., Boccaccini, A.R., 2013. Review. Functional glasses and glass-ceramics derived from iron rich waste and combination of industrial residues. J. Non-Cryst. Solids 365, 63–74. https://doi.org/10.1016/j.jnoncrysol.2012.12.006.
Cicconi, M.R., Le Losq, C., Moretti, R., Neuville, D.R., 2020. Magmas are the largest repositories and carriers of earth's redox processes. Elements 16, 173–178. https://doi.org/10.2138/GSELEMENTS.16.3.173.
Dalby, K.N., King, P.L., 2006. A new approach to determine and quantify structural units in silicate glasses using micro-reflectance Fourier-Transform infrared spectroscopy. Am. Mineral. 91, 1783–1793. https://doi.org/10.2138/am.2006.2075.
Di Genova, D., Hess, K.U., Chevrel, M.O., Dingwell, D.B., 2016. Models for the estimation of Fe^{3+}/Fe_{tot} ratio in terrestrial and extraterrestrial alkali- and iron-rich silicate glasses using Raman spectroscopy. Am. Mineral. 101, 943–952. https://doi.org/10.2138/am-2016-5534CCBYNCND.
Di Genova, D., Vasseur, J., Hess, K.U., Neuville, D.R., Dingwell, D.B., 2017. Effect of oxygen fugacity on the glass transition, viscosity and structure of silica- and iron-rich magmatic melts. J. Non-Cryst. Solids 470, 78–85. https://doi.org/10.1016/j.jnoncrysol.2017.05.013.
Di Genova, D., Brooker, R.A., Mader, H., Drewitt, J.W.E., Longo, A., Deubener, J., Neuville, D.R., Fanara, S., Shebanova, O., Anzellini, S., Arzilli, F., Bamber, E.C., Hennet, L., La Spina, G., Miyajima, N., 2020. In situ observation of nanolite growth in volcanic melt: a driving force for explosive eruptions. Sci. Adv. 6, 1–13.
Di Muro, A., Métrich, N., Mercier, M., Giordano, D., Massare, D., Montagnac, G., 2009. Micro-Raman determination of iron redox state in dry natural glasses: Application to peralkaline rhyolites and basalts. Chem. Geol. 259, 78–88. https://doi.org/10.1016/j.chemgeo.2008.08.013.
Falenty, K., Webb, S.L., 2010. Shear modulus, heat capacity, viscosity and structural relaxation time of Na_2O-Al_2O_3-SiO_2 and Na_2O-Fe_2O_3-Al_2O_3-SiO_2 melts. Phys. Chem. Miner. 37, 613–634. https://doi.org/10.1007/s00269-010-0362-7.
Farges, F., Lefrère, Y., Rossano, S., Berthereau, A., Calas, G., Brown, G.E., 2004. The effect of redox state on the local structural environment of iron in silicate glasses: a combined XAFS spectroscopy, molecular dynamics, and bond valence study. J. Non-Cryst. Solids 344, 176–188. https://doi.org/10.1016/j.jnoncrysol.2004.07.050.
Galeener, F.L., 1979. Band limits and the vibrational spectra of tetrahedral glasses. Phys. Rev. B 19, 4292–4297. https://doi.org/10.1103/PhysRevB.19.4292.
Giordano, D., Dingwell, D.B., 2003. Non-Arrhenian multicomponent melt viscosity: a model. Earth Planet. Sci. Lett. 208, 337–349. https://doi.org/10.1016/S0012-821X(03)00042-6.
Giordano, D., Mangiacapra, A., Potuzak, M., Russell, J.K., Romano, C., Dingwell, D.B., Di Muro, A., 2006. An expanded non-Arrhenian model for silicate melt viscosity: a treatment for metaluminous, peraluminous and peralkaline liquids. Chem. Geol. 229, 42–56. https://doi.org/10.1016/j.chemgeo.2006.01.007.
Giordano, D., Polacci, M., Papale, P., Caricchi, L., 2010. Rheological control on the dynamics of explosive activity in the 2000 summit eruption of Mt. Etna. Solid Earth 1, 61–69. https://doi.org/10.5194/se-1-61-2010.
Giordano, D., Vona, A., Gonzalez-Garcia, D., Allabar, A., Kolzenburg, S., Polo, L., de Janasi Assis Janasic, V., Behrens, H., De Campos, C.P., De Cristofaro, S., Freitas Guimaraesc, L., Freitas, L., Nowak, M., Müller, D., Günther, A., Masotta, M., Roverato, M., Romano, C., Dingwell, D.B., 2021. Viscosity of Palmas-type magmas of the Paraná Magmatic Province (Rio Grande do Sul State, Brazil): Implications for high-temperature silicic volcanism. Chem. Geol. 560. https://doi.org/10.1016/j.chemgeo.2020.119981.
González-García, D., Giordano, D., Russell, J.K., Dingwell, D.B., 2020. A Raman spectroscopic tool to estimate chemical composition of natural volcanic glasses. Chem. Geol. 556, 119819. https://doi.org/10.1016/j.chemgeo.2020.119819.
Hehlen, B., Neuville, D.R., 2020. Non network-former cations in oxide glasses spotted by Raman scattering. Phys. Chem. Chem. Phys. 22, 12724–12731. https://doi.org/10.1039/d0cp00630k.
Hehlen, B., Neuville, D.R., Kilymis, D., Ispas, S., 2017. Bimodal distribution of Si–O–Si angles in Sodo-silicate glasses. J. Non-Cryst. Solids 469, 39–44. https://doi.org/10.1016/j.jnoncrysol.2017.04.009.
Hemmati, M., Angell, C.A., 1997. IR absorption of silicate glasses studied by ion dynamics computer simulation. I. IR spectra of SiO_2 glass in the rigid ion model approximation. J. Non-Cryst. Solids 217, 236–249. https://doi.org/10.1016/S0022-3093(97)00135-X.
Holland, D., Mekki, A., Gee, I.A., McConville, C.F., Johnson, J.A., Johnson, C.E., Appleyard, P., Thomas, M., 1999. Structure of sodium iron silicate glass - a multi-technique approach. J. Non-Cryst. Solids 253, 192–202. https://doi.org/10.1016/S0022-3093(99)00353-1.
Hornby, A.J., Ayris, P.M., Damby, D.E., Diplas, S., Eychenne, J., Kendrick, J.E., Cimarelli, C., Kueppers, U., Scheu, B., Utley, J.E.P., Dingwell, D.B., 2024. Nanoscale silicate melt textures determine volcanic ash surface chemistry. Nat. Commun. 15, 1–10. https://doi.org/10.1038/s41467-024-44712-6.
Jochum, K.P., Stoll, B., Herwig, K., Willbold, M., Hofmiann, A.W., Amini, M., Aarburg, S., Abouchami, W., Hellebrand, E., Mocek, B., et al., 2006. MPI-DING reference glasses for in situ microanalysis: New reference values for element concentrations and isotope ratios. Geochem. Geophys. Geosyst. 7, 2.
Jones, T.J., Le Moigne, Y., Russell, J.K., Williams-Jones, G., Giordano, D., Dingwell, D.B., 2022a. Inflated pyroclasts in proximal fallout deposits reveal abrupt transitions in eruption behaviour. Nat. Commun. 13, 1–12. https://doi.org/10.1038/s41467-022-30501-6.
Jones, T.J., Russell, J.K., Brown, R.J., Hollendonner, L., 2022b. Melt stripping and agglutination of pyroclasts during the explosive eruption of low viscosity magmas. Nat. Commun. 13. https://doi.org/10.1038/s41467-022-28633-w.
Kalampounias, A.G., Yannopoulos, S.N., Papatheodorou, G.N., 2006. A high-temperature Raman spectroscopic investigation of the potassium tetrasilicate in glassy, supercooled, and liquid states. J. Chem. Phys. 125. https://doi.org/10.1063/1.2360275.
Lalonde, A.E., Rancourt, D.G., Ping, J.Y., 1998. Accuracy of ferric/ferrous determinations in micas: a comparison of Mössbauer spectroscopy and the Pratt and Wilson wet-chemical methods. Hyperfine Interact. 117, 175–204.
Le Losq, C., Neuville, D.R., Florian, P., Henderson, G.S., Massiot, D., 2014. The role of Al^{3+} on rheology and structural changes in sodium silicate and aluminosilicate glasses and melts. Geochim. Cosmochim. Acta 126, 495–517. https://doi.org/10.1016/j.gca.2013.11.010.
Le Losq, C., Berry, A.J., Kendrick, M.A., Neuville, D.R., O'Neill, H.S.C., 2019. Determination of the oxidation state of iron in Mid-Ocean Ridge basalt glasses by Raman spectroscopy. Am. Mineral. 104, 1032–1042. https://doi.org/10.2138/am-2019-6887.
Le Losq, C., Cicconi, M.R., Neuville, D.R., 2021. Iron in silicate glasses and melts: Implications for volcanological processes. Magma Redox Geochemistry 233–253. https://doi.org/10.1002/9781119473206.ch12.
Liebske, C., Behrens, H., Holtz, F., Lange, R.A., 2003. The influence pf pressure and composition on the viscocity of andesitic melts. Geochim. Cosmochim. Acta 67, 473–485. https://doi.org/10.1016/S0016-7037(02)01139-0.
Malinovsky, V.K., Novikov, V.N., Sokolov, A.P., 1991. Log-normal spectrum of low-energy vibrational excitations in glasses. Phys. Lett. A 153, 63–66. https://doi.org/10.1016/0375-9601(91)90363-D.
Matson, D.W., Sharma, S.K., Philpotts, J.A., 1983. The structure of high-silica alkali-silicate glasses. A Raman spectroscopic investigation. J. Non-Cryst. Solids 58, 323–352. https://doi.org/10.1016/0022-3093(83)90032-7.
McMillan, P., Piriou, B., 1983. Raman spectroscopic studies of silicate and related glass structure: a review. Bull. Mineral. 106, 57–75. https://doi.org/10.3406/bulmi.1983.7668.
Mysen, B.O., 2006. The structural behavior of ferric and ferrous iron in aluminosilicate glass near meta-aluminosilicate joins. Geochim. Cosmochim. Acta 70, 2337–2353. https://doi.org/10.1016/j.gca.2006.01.026.
Mysen, B.O., Richet, P., 2005. Silicate glasses and melts - Properties and structure. Developments in Geochemistry, vol. 10. Elsevier, pp. 291–354.
Mysen, B., Seifert, F., Virgo, D., 1980. Structure and redox equilibria of iron-bearing silicate melts. Am. Mineral. 65, 867–884.
Mysen, B.O., Virgo, D., Scarfe, C.M., Cronin, D.J., 1985. Viscosity and structure of iron- and aluminum-bearing calcium silicate melts at 1 atm. Am. Mineral. 70, 487–498.
Neave, D.A., 2020. Chemical variability in peralkaline magmas and magma reservoirs: insights from the Khaggiar lava flow, Pantelleria. Italy. Contrib. to Mineral. Petrol. 175. https://doi.org/10.1007/s00410-020-01678-0.
Nodari, L., Conte, S., Casini, L., Sisti, M., Fantini, R., Gualtieri, A.F., Molinari, C., Zanelli, C., Giordano, D., Dondi, M., Arletti, R., 2025. Role of iron-rich clays on sintering of porcelain stoneware tiles. J. Eur. Ceram. Soc. 45. https://doi.org/10.1016/j.jeurceramsoc.2024.116947.
Okumura, S., Uesugi, K., Goto, A., Sakamaki, T., Matsumoto, K., Takeuchi, A., Miyake, A., 2022. Rheology of nanocrystal-bearing andesite magma and its roles in explosive volcanism. Commun. Earth Environ. 3, 1–8. https://doi.org/10.1038/s43247-022-00573-9.
Rancourt, D.G., Ping, J.Y., 1991. Voigt-based methods for arbitrary-shape static hyperfine parameter distributions in Mössbauer spectroscopy. Nucl. Inst. Methods Phys. Res. B 58, 85–97. https://doi.org/10.1016/0168-583X(91)95681-3.
Richet, P., Neuville, D.R., 1992. Thermodynamics of Silicate Melts: Configurational Properties. Thermodyn. data 132–161. https://doi.org/10.1007/978-1-4612-2842-4_5.
Ritz, M., 2023. Infrared and Raman Spectroscopy of Mullite Ceramics Synthesized from Fly Ash and Kaolin. Minerals 13. https://doi.org/10.3390/min13070864.
Rossano, S., Ramos, A.Y., Delaye, J.M., 2000. Environment of ferrous iron in CaFeSi2O6 glass; contributions of EXAFS and molecular dynamics. J. Non-Cryst. Solids 273, 48–52. https://doi.org/10.1016/S0022-3093(00)00124-1.
Rouxel, T., 2007. Elastic properties and short-to medium-range order in glasses. J. Am. Ceram. Soc. 90, 3019–3039. https://doi.org/10.1111/j.1551-2916.2007.01945.x.
Shannon, R.D., 1976. Revised effective ionic radii and systematic studies of interatomic distances in halides and chalcogenides. Acta Crystallogr. Sect. A 32, 751–767. https://doi.org/10.1107/S0567739476001551.
Shuker, R., Gammon, R.W., 1970. Raman-scattering selection-rule breaking and the density of states in amorphous materials. Phys. Rev. Lett. 25, 222–225. https://doi.org/10.1103/PhysRevLett.25.222.
Stabile, P., Webb, S., Knipping, G.L., Behrens, H., Paris, E., Giuli, G., 2016. Viscosity of pantelleritic and alkali-silicate melts: Effect of Fe redox state and Na/(Na+K) ratio. Chem. Geol. 442, 73–82. https://doi.org/10.1016/j.chemgeo.2016.09.003.
Szewczyk, D., Cassetta, M., 2024. Colossal low-temperature upturn in the heat capacity of volcanic glasses. J. Non-Cryst. Solids 637, 123046. https://doi.org/10.1016/j.jnoncrysol.2024.123046.
Tasheva, T., Harizanova, R., Mihailova, I., Cherkezova-Zheleva, Z., Paneva, D., Nedkova, M., Rüssel, C., 2023. Structure and redox ratio of soda-lime-silica glasses with high iron oxide concentrations. Int. J. Appl. Glas. Sci. 14, 445–454. https://doi.org/10.1111/ijag.16626.

Toplis, M.J., Dingwell, D.B., Hess, K.U., Lenci, T., 1997. Viscosity, fragility, and configurational entropy of melts along the join SiO_2-$NaAlSiO_4$. Am. Mineral. 82, 979–990. https://doi.org/10.2138/am-1997-9-1014.

Webb, S.L., 2021. Viscosity of evolving magmas: a case study of the Glass House Mountains. Australia. Bull. Volcanol. 83. https://doi.org/10.1007/s00445-021-01495-8.

Wilke, M., 2005. Fe in magma - An overview. Ann. Geophys. 48, 609–617. https://doi.org/10.4401/ag-3222.

Wilke, M., Farges, F., Partzsch, G.M., Schmidt, C., Behrens, H., 2007. Speciation of Fe in silicate glasses and melts by in-situ XANES spectroscopy. Am. Mineral. 92, 44–56. https://doi.org/10.2138/am.2007.1976.

Zanatta, M., Baldi, G., Caponi, S., Fontana, A., Gilioli, E., Krish, M., Masciovecchio, C., Monaco, G., Orsingher, L., Rossi, F., Ruocco, G., Verbeni, R., 2010. Elastic properties of permanently densified silica: a Raman, Brillouin light, and x-ray scattering study. Phys. Rev. B 81, 4–7. https://doi.org/10.1103/PhysRevB.81.212201.

Zimova, M., Webb, S., 2006. The effect of chlorine on the viscosity of Na_2O-Fe_2O_3-Al_2O_3-SiO_2 melts. Am. Mineral. 91, 344–352. https://doi.org/10.2138/am.2006.1799.